Porous Molybdenum-Based Hybrid Catalysts for Highly Efficient Hydrogen Evolution

Yu-Jia Tang, Min-Rui Gao, Chun-Hui Liu, Shun-Li Li, Hai-Long Jiang, Ya-Qian Lan,* Min Han, and Shu-Hong Yu*

Abstract: *We have synthesized a porous Mo-based composite obtained from a polyoxometalate-based metal–organic framework and graphene oxide (POMOFs/GO) using a simple one-pot method. The MoO_2@PC-RGO hybrid material derived from the POMOFs/GO composite is prepared at a relatively low carbonization temperature, which presents a superior activity for the hydrogen-evolution reaction (HER) in acidic media owing to the synergistic effects among highly dispersive MoO_2 particles, phosphorus-doped porous carbon, and RGO substrates. MoO_2@PC-RGO exhibits a very positive onset potential close to that of 20% Pt/C, low Tafel slope of $41\,mV\,dec^{-1}$, high exchange current density of $4.8 \times 10^{-4}\,A\,cm^{-2}$, and remarkable long-term cycle stability. It is one of the best high-performance catalysts among the reported nonprecious metal catalysts for HER to date.*

$\mathbf{H}$ydrogen (H_2), as a renewable and environment-friendly energy, has triggered broad attention to replace the fossil fuels because of the increasingly serious energy crisis and environmental contamination.[1] Producing H_2 from electrocatalytic splitting of water by the hydrogen-evolution reaction (HER) has become a research focus because of the high efficiency of energy conversion.[2] Pt group metals are the state-of-the-art catalysts to generate H_2 with high current density at low overpotential (η) in acidic media. However, the scarcity, high costs, and the instability of Pt limits the widespread application for the HER.[3] Recently, non-noble electrocatalysts have been widely studied, such as transition-metal sulfides,[4] carbides,[5] phosphides,[6] and nitrides,[7] which show the promising future when Pt-based catalysts will be replaced.

Molybdenum dioxide (MoO_2) is an unusual transition-metal oxide that has a high metallic-like electrical conductivity and high stability, which has received much attention

recently.[8] Besides, the Mo edge and O edge are both active sites of MoO_2 which is the key factor that renders MoO_2 a HER catalyst. However, MoO_2 has been reported rarely as HER electrocatalysts because MoO_2 is limited by an aggregation phenomenon and few exposed active sites.[9] To avoid the aggregation of nanoparticles, substrates such as porous carbon and graphene have been introduced into metal-based catalysts for multiple catalytic reactions. On this basis, if the number of exposed active sites was increased, we could prepare stable and highly dispersive MoO_2/C or MoO_2/GO catalysts for the HER. Most recently, metal-free doped carbon materials have shown relatively high electrocatalytic activities for the HER.[10] These materials have long-term durability and abundant exposed active sites since the heteroatom (N, P, S) is covalently bound within the carbon framework. As such, the combination of MoO_2 and heteroatom-doped carbon materials not only prevents the aggregation of MoO_2, but also increases the accessible number of active sites. Especially, phosphorus-doped materials display an excellent catalytic performance because phosphorus has lone-pair electrons in 3p orbitals and vacant 3d orbitals, and can accommodate the surface charge state and induce local charge density.[7c, 11] Therefore, it is a very significant subject to prepare effective HER catalysts in combination with MoO_2 and P-doped carbon substrates.

Polyoxometalate (POM)-based metal–organic frameworks (MOFs) have been synthesized in quantity by researchers, which contain POM units and metal–organic fragments forming the intriguing structures and show potential applications in catalysis.[12] Recently, novel classes of porous carbon materials, metal oxides and their nanocomposites derived from MOFs have been reported as electrocatalysts for the oxygen-reduction reaction (ORR) or electrode materials for Li-ion batteries and supercapacitors.[13] Our group not only focuses on the study of POMOFs crystals,[14] but also has reported heteroatom-doped metal-free carbon materials using MOFs as templates for electrocatalysts.[15] To date, only Lou's group choses POMOFs as precursors to prepare nanostructured MoC_x for the HER.[5b] Hence, we predict that POMOFs can be carbonized to obtain chemically doped porous carbon-coated nanosized transition-metal (Mo, W, V from polyoxometalate) oxides or carbides. This idea integrates the non-noble metal materials with heteroatom-doped carbon materials tactfully.

In this work, we firstly synthesized the POMOFs/GO composite using $H_3PMo_{12}O_{40} \cdot n\,H_2O$ (PMo_{12}), $Cu(OAc)_2 \cdot H_2O$, H_3BTC, and graphene oxide (GO) as precursors by a simple one-pot method (OAc = acetat and H_3BTC = 1,3,5-benzene-tricarboxylic acid). The composites combine the advantages

[*] Dr. Y.-J. Tang,[+] Dr. C.-H. Liu, Prof. S.-L. Li, Prof. Y.-Q. Lan, Prof. M. Han
School of Chemistry and Materials Science
Nanjing Normal University, Nanjing 210023 (P.R. China)
E-mail: yqlan@njnu.edu.cn

Dr. M.-R. Gao,[+] Prof. H.-L. Jiang, Prof. S.-H. Yu
Division of Nanomaterials and Chemistry, Hefei National Laboratory for Physical Sciences at Microscale, Collaborative Innovation Center of Suzhou, Nano Science and Technology, Department of Chemistry, University of Science and Technology of China
Hefei 230026 (P.R. China)
E-mail: shyu@ustc.edu.cn

[+] These authors contributed equally to this work.

Supporting information for this article is available on the WWW under http://dx.doi.org/10.1002/anie.201505691.

of POMs, MOFs, and GO. POMOFs crystals are well dispersed on GO, which benefit from the use of electrostatic interactions to attach anionic PMo_{12} to negatively charged GO sheets. Then, we synthesized a new hybrid material consisting of MoO_2, phosphorus-doped nanoporous carbon, and RGO substrates (denoted as MoO_2@PC-RGO) using a POMOFs/GO-assisted strategy for the following considerations: First, PMo_{12} can function as the molybdenum and phosphorus source. Second, graphene sheets are one of the most promising components as support for electrocatalysts because of their good conductivity, large surface area, and high stability.[16] Third, the agglomeration of MoO_2 can be avoided by confining the carbon skeleton, and MoO_2@PC hybrids are loaded onto RGO uniformly because of the distinct structure of the POMOFs/GO composite. Phosphorus (0.37 at.%) is doped with MoO_2@PC-RGO through P−O and P−C bonds, which are not negligible and increase the catalytic activity. Overall, the MoO_2@PC-RGO nanocomposite displays an excellent HER activity in acidic media, with the onset potential close to 0 mV (vs. the reversible hydrogen electrode, RHE), approaching that of commercial 20% Pt/C.

POMOFs (NENU-5)[17] was chosen as the precursor and GO was introduced to prepare nanosized POMOFs/GO composites first. As shown in Scheme 1, GO was mixed with
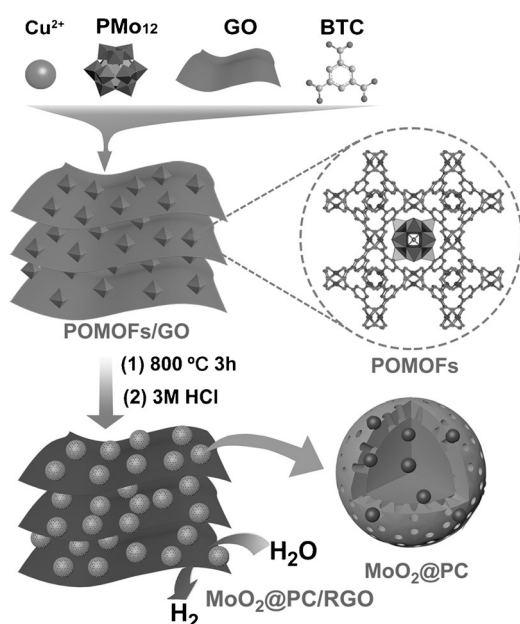
Scheme 1. Preparation process of the MoO_2@PC-RGO nanocomposite used as electrocatalyst for the HER.

$Cu(OAc)_2 \cdot H_2O$ and PMo_{12} in distilled water and then H_3BTC was added dropwise under continuous stirring at room temperature. Meanwhile, the solution turned turbid and green with the rapid formation of POMOFs/GO (GO loadings are 3, 8, and 15 wt%). The powder X-ray diffraction (PXRD) patterns of nano-POMOFs and POMOFs/GO (8 wt%) confirm the phase purity and good crystallinity (see Figure S2 in the Supporting Information). Upon heat treatment of nano-POMOFs and POMOFs/GO under N_2

atmosphere at 800°C for 3 h, Cu/MoO_2@PC and Cu/MoO_2@PC-RGO were obtained and then washed with 3 M hydrochloric acid (HCl) and distilled water to remove the metallic Cu nanoparticles. Although MoO_2 and Mo_2C are known as both possible products that were synthesized by carbonizing nano-POMOFs or POMOFs/GO in an inert atmosphere, we can get the target product—MoO_2@PC-RGO by accurately controlling the carbonization temperature and time (see Experimental Section and Figure S3a). At the same time, GO sheets were transformed to RGO nanosheets because of the decrease in oxygenic groups and the redox reaction during the thermal treatment. The Raman spectrum was tested before and after thermal treatment and proved the above-mentioned results (Figure S3b).

A transmission electron microscopy (TEM) image of POMOFs/GO (8 wt%) is shown in Figure 1a. Clearly, POMOF nanocrystals are rhombic (ca. 100 nm in size) and uniformly loaded onto GO nanosheets. After thermal and acid treatment, the morphology of the MoO_2@PC-RGO nanocomposite (Figure 1b) is different from original crystals but still distributed on RGO sheets uniformly. This change is
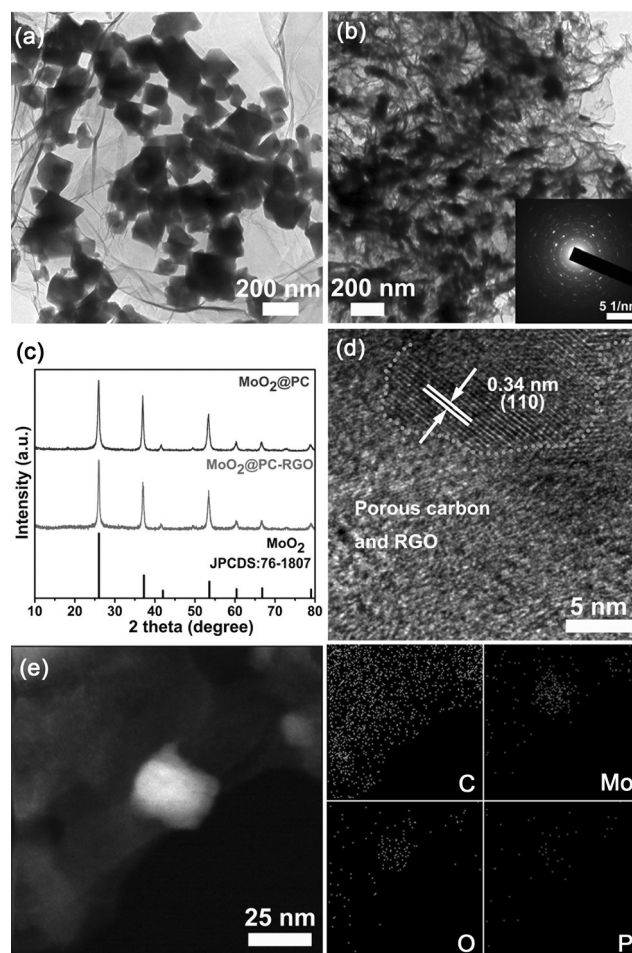

Figure 1. TEM images of a) POMOFs/GO (8 wt%) and b) MoO_2@PC-RGO. c) PXRD patterns of as-prepared MoO_2@PC and MoO_2@PC-RGO. d) HRTEM image of MoO_2@PC-RGO (8 wt%). e) Corresponding EDX elemental mapping of C, Mo, O, and P. The inset in (b) shows a SAED pattern.

due to the aggregation and growth of MoO_2@PC during the sintering process. TEM and the emission scanning electron microscopy (SEM) images of MoO_2@PC and MoO_2@PC-RGO are corresponding to the above results (Figure S4). In addition, the morphology of POMOFs/GO with different loadings of GO (0, 3, 8, 15 wt%) are also characterized by TEM and SEM (Figures S5 and S6). POMOFs/GO (8 wt%) shows the most homogeneous distributions on GO nanosheets.

The high-resolution TEM (HRTEM) image of MoO_2@PC-RGO is shown in Figure 1d, in which a lattice spacing of 0.34 nm is observed, consistent with the *d* spacing of the (110) planes of MoO_2. Besides, the selected-area electron diffraction (SAED) pattern (inset in Figure 1b) displays the individual spots associated with concentric rings, indicating the polycrystalline nature of MoO_2@PC-RGO. As shown in Figure 1e, elemental mapping has been employed to obtain the elemental distribution of C, Mo, O, and P in the composites, verifying MoO_2 particles embedded in porous carbon and RGO nanosheets, where the P element is mainly distributed around MoO_2 in accord with the structure of POMOFs.

PXRD patterns of MoO_2@PC-RGO and MoO_2@PC are shown in Figure 1c, which is consistent with JPCDS card number 76-1807 for the pure monoclinic phase of MoO_2. No other diffraction peaks are determined for impurities and as-prepared MoO_2 displays a good crystallinity. Elemental copper is characterized by a PXRD pattern before being washed by 3 M HCl (Figure S7). This result is further confirmed by an energy-dispersive X-ray (EDX) spectrum (Figure S8). The EDX spectrum shows the presence of C, Mo, O, and P of MoO_2@PC-RGO. No peaks for Cu elements are detected. X-ray photoelectron spectroscopy (XPS) can be used to characterize the atomic valence state and composition. Details can be seen in the Supporting Information (Figures S9 and S10).

MoO_2@PC and MoO_2@PC-RGO (8 wt%) hybrid materials were investigated as electrocatalysts for the HER (All polarization curves are not corrected for IR loss). Figure 2a shows the polarization curves (sample loading: 0.14 mg cm^{-2}) in N$_2$-saturated 0.5 M H$_2$SO$_4$ with a scan rate of 5 mV s^{-1}. MoO_2@PC has an onset potential of about 66 mV. After introducing RGO sheets, the constructed MoO_2@PC-RGO was unexpectedly found to start the H$_2$ evolution near its thermodynamic potential (i.e., 0 mV), approaching the performance of high-grade Pt/C catalyst. The operating η values at a current density of 10 mA cm^{-2} (η_{10}, Table 1) are measured to be 38 mV for 20% Pt/C, 64 mV for MoO_2@PC-RGO, and 136 mV for MoO_2@PC. In addition, MoO_2@PC catalysts prepared at different temperatures are assessed and the sample prepared at 800 °C exhibits the highest HER activity (Figure S11). When GO (8 wt%) exists in MoO_2@PC-RGO, this composite catalyst exhibits an optimum HER activity (Figure S12). Moreover, removing Cu from the composite structure can further permit HER performance gains (Figure S13). Compared with the physical mixture of commercial MoO_2 and acetylene black (MoO_2-AB), the MoO_2@PC catalyst shows a dramatically enhanced HER performance possibly because of the use of POMOFs as precursors, which
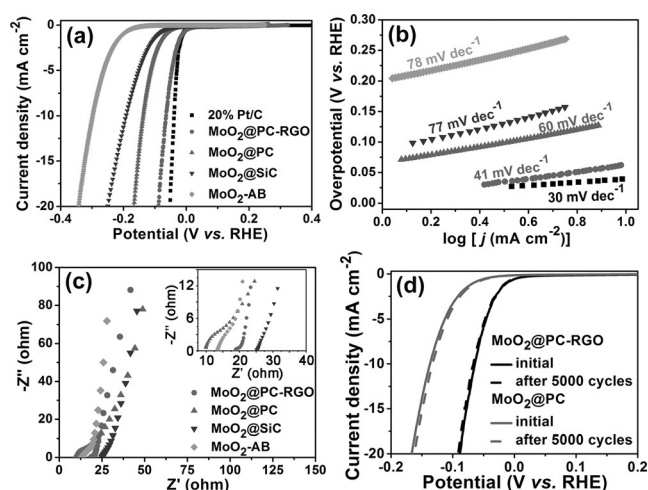

Figure 2. a) Polarization curves for four electrocatalysts and 20% Pt/C. b) Tafel plots of the corresponding polarization curves. c) Electrochemical impedance spectra (EIS) of four electrocatalysts. d) Durability measurements with MoO_2@PC-RGO and MoO_2@PC.

Table 1: Comparison of catalytic parameters of different HER catalysts.

Catalyst	Onset Potential [mV][a]	Tafel slope [mV dec^{-1}]	η_{10} [mA cm^{-2}][a]	j_0 [A cm^{-2}][b]
20% Pt/C	ca. 0	30	38	3.9×10^{-4}
MoO_2@PC-RGO	ca. 0	41	64	4.8×10^{-4}
MoO_2@PC	66	60	136	8.2×10^{-5}
MoO_2@SiC	85	77	191	7.2×10^{-5}
MoO_2-AB	174	78	297	2.7×10^{-6}

[a] The potential measured versus RHE. [b] j_0 values were calculated from Tafel curves using an extrapolation method.

can form porous carbon with large areas and hierarchical pores. In addition, a little amount of P doped in MoO_2@PC also provides a positive contribution to the measured remarkable HER activity. To verify this, we synthesized MoO_2@SiC by using the same POMOFs structure (NENU-4)[16] except that H$_3$SiMo$_{12}$O$_{40}$ was used to replace H$_3$PMo$_{12}$O$_{40}$. It clearly shows that MoO_2@PC has a more positive onset potential value and η_{10} than those of MoO_2@SiC, proving the important role of phosphorus doping for the HER (Figure 2a). Strikingly, our developed MoO_2@PC-RGO catalysts shows excellent HER activity, which is better than any other reported non-precious metal catalysts, such as MoS$_2$,[4a] Mo$_2$C,[5b] Ni$_2$P,[6a] Cu$_3$P,[6b] and P-WN/RGO[7c] (Table S3).

The HER kinetics of the above-mentioned catalysts was further evaluated by corresponding Tafel plots (log$j \sim \eta$). As shown in Figure 2b, Tafel slopes of 30, 41, 60, 77, and 78 mV dec^{-1} are measured for commercial 20% Pt/C, MoO_2@PC-RGO, MoO_2@PC, MoO_2@SiC, and MoO_2-AB catalysts, respectively. According to the mechanism of hydrogen evolution, there are three principal steps for the HER in acidic electrolytes, including the Volmer, the Heyrovsky, and the Tafel steps.[18] Thus, the measured Tafel slope of

$41\ mV\,dec^{-1}$ for the MoO$_2$@PC-RGO composite suggests a Volmer–Heyrovsky mechanism that has an effect in this catalyst, where the electrochemical desorption is the rate-limiting step.

Exchange current density (j_0), the most inherent measure of HER activity, is also carefully calculated to evaluate the level of the MoO$_2$@PC-RGO catalyst (Table 1 and Figure S14). Remarkably, the exchange current density of MoO$_2$@PC-RGO ($4.8 \times 10^{-4}\ A\,cm^{-2}$) is higher than that of commercial 20% Pt/C catalyst ($3.9 \times 10^{-4}\ A\,cm^{-2}$) and higher than most of the reported non-precious metal HER catalysts (Table S3). We further measured the electrochemical double-layer capacitance (EDLC, C_{dll}) of the studied catalysts by using a cyclic voltammetry (CV) method to evaluate the electrochemically active surface areas (Figure S15).[19] The C_{dll} values of MoO$_2$@PC-RGO and MoO$_2$@PC are 131.2 and $19.2\ mF\,cm^{-2}$, respectively. Thus, MoO$_2$@PC-RGO has a much higher electrochemically active surface area than MoO$_2$@PC which is associated with its large exchange current density. Moreover, the larger surface roughness of MoO$_2$@PC-RGO exhibits more exposed edges and proliferative active sites, determining its outstanding HER activity.

We then applied electrochemical impedance spectra (EIS) to provide further insight into the electrode kinetics of the studied catalysts (Figure 2c). A simplified equivalent circuit (Figure S16) is used to explain the measured results. As can be seen in Figure 2c, these plots are all composed of a semicircle at high-frequency regions and a vertical line at low-frequency regions (the inset in Figure 2c shows a larger version of the high-frequency regions). The charge-transfer resistance (R_{ct}) value is $2.21\ \Omega$ for MoO$_2$@PC-RGO, which is much lower than that of the other three catalysts (more parameters are listed in Table S2), suggesting a highly efficient electron transport and favorable HER kinetics at the MoO$_2$@PC-RGO/electrolyte interface. The long-term stability of the MoO$_2$@PC-RGO and MoO$_2$@PC catalysts has been studied and Figure 2d shows that MoO$_2$@PC-RGO has only a little deterioration of cathodic currents after 5000 cycles and the currents of MoO$_2$@PC even increase slightly. The results indicate that the catalysts of the acidic electrode show some minor corrosion. Moreover, chronoamperometry (CA) for MoO$_2$@PC-RGO and MoO$_2$@PC was also tested (Figure S17). The remarkable long-term stability of MoO$_2$@PC-RGO is attributed to the tightly wrapped MoO$_2$ particles by P-doped carbon and RGO, which protects MoO$_2$ against oxidation by air.

The superior catalytic performance of MoO$_2$@PC-RGO could be attributed to the synergistic effects among the conductive RGO support, nanosized MoO$_2$ particles, phosphorus-doped carbon skeleton as well as the closely interconnected network. First, serving as the support matrix, RGO nanosheets could increase the electrochemical conductivity and surface area and improve the HER activity of the MoO$_2$@PC-RGO catalyst substantially. Second, nano-POMOFs crystals were chosen as the template to fabricate small-sized MoO$_2$ particles embedded in carbon skeleton. This unique structure derived from nano-POMOFs prevents MoO$_2$ particles from aggregation and thus provides more exposed Mo edges and O edges. Notably, MoO$_2$ particles play

a key role to improve HER performance because MoO$_2$ particles offer abundant active sites to promote hydrogen adsorption and desorption quickly in acid electrolyte. Third, a phosphorus source derived from PMo$_{12}$ in POMOFs plays an indispensable role in the HER performance. In accord with the HER tests, introducing phosphorus into metal/carbon composites brings about a low Tafel slope and η_{10} value during the electrocatalytic process in contrast with silicon-doping MoO$_2$@SiC sample. In addition, the porous structure obtained by heat treatment ensures easy contact to the electrolyte and more exposed active sites to promote the hydrogen production process.

In summary, we have successfully synthesized a new hybrid material MoO$_2$@PC-RGO by pyrolyzing a POMOFs/GO composite for the first time. The nano-POMOFs crystals have unique structures that prevents aggregation of the MoO$_2$ nanoparticles, which are embedded in a phosphorus-doped carbon skeleton, during thermal treatment. Besides, introducing GO into POMOFs not only improves the conductivity and electrocatalytic activity of MoO$_2$@PC-RGO, but also plays an important role as support for the formation of a closely interconnected network. Owing to the synergistic effects among highly dispersive MoO$_2$ particles, phosphorus-doped porous carbon and RGO substrates, the MoO$_2$@PC-RGO nanocomposite shows a remarkable HER activity with a small onset potential of about 0 mV, a low Tafel slope of $41\ mV\,dec^{-1}$, a high exchange current density of $4.83 \times 10^{-4}\ A\,cm^{-2}$, and long-term stability in acidic media. It is one of the best high-performance catalysts among the reported non-precious metal catalysts for the HER to date. We believe that this strategy is also suitable for the synthesis of other nanoscale non-noble metal oxides or carbides confined in heteroatom-doped carbon skeletons used as highly efficient electrocatalysts for the HER and ORR.

Acknowledgements

[1] a) M. S. Dresselhaus, I. L. Thomas, *Nature* **2001**, *414*, 332–337; b) J. A. Turner, *Science* **2004**, *305*, 972–974.

[2] a) E. Antolini, *Energy Environ. Sci.* **2009**, *2*, 915–931; b) M. G. Walter, E. L. Warren, J. R. McKone, S. W. Boettcher, Q. Mi, E. A. Santori, N. S. Lewis, *Chem. Rev.* **2010**, *110*, 6446–6473.

[3] J. R. McKone, E. L. Warren, M. J. Bierman, S. W. Boettcher, B. S. Brunschwig, N. S. Lewis, H. B. Gray, *Energy Environ. Sci.* **2011**, *4*, 3573–3583.

[4] a) J. Xie, H. Zhang, S. Li, R. Wang, X. Sun, M. Zhou, J. Zhou, X. W. Lou, Y. Xie, *Adv. Mater.* **2013**, *25*, 5807–5813; b) M.-R. Gao, J.-X. Liang, Y.-R. Zheng, Y.-F. Xu, J. Jiang, Q. Gao, J. Li, S.-H. Yu, *Nat. Commun.* **2015**, *6*, 5982–5988; c) X. Huang, Z. Zeng, S. Bao, M. Wang, X. Qi, Z. Fan, H. Zhang, *Nat. Commun.* **2013**, *4*, 1444–1451.

[5] a) P. Xiao, X. Ge, H. Wang, Z. Liu, A. Fisher, X. Wang, *Adv. Funct. Mater.* **2015**, *25*, 1520–1526; b) H.-B. Wu, B.-Y. Xia, L. Yu, X.-Y. Yu, X.-W. Lou, *Nat. Commun.* **2015**, *6*, 6512–6519; c) Y. Yan, B. Xia, X. Qi, H. Wang, R. Xu, J.-Y. Wang, H. Zhang, X. Wang, *Chem. Commun.* **2013**, *49*, 4884–4886; d) D. V. Esposito, S. T. Hunt, A. L. Stottlemyer, K. D. Dobson, B. E. McCandless, R. W. Birkmire, J. G. Chen, *Angew. Chem. Int. Ed.* **2010**, *49*, 9859–9862; *Angew. Chem.* **2010**, *122*, 10055–10058.

[6] a) E. J. Popczun, J. R. McKone, C. G. Read, A. J. Biacchi, A. M. Wiltrout, N. S. Lewis, R. E. Schaak, *J. Am. Chem. Soc.* **2013**, *135*, 9267–9270; b) J. Tian, Q. Liu, N. Cheng, A. M. Asiri, X. Sun, *Angew. Chem. Int. Ed.* **2014**, *53*, 9577–9581; *Angew. Chem.* **2014**, *126*, 9731–9735.

[7] a) J. Xie, S. Li, X. Zhang, J. Zhang, R. Wang, H. Zhang, B. Pan, Y. Xie, *Chem. Sci.* **2014**, *5*, 4615–4620; b) B. Cao, G. M. Veith, J. C. Neuefeind, R. R. Adzic, P. G. Khalifah, *J. Am. Chem. Soc.* **2013**, *135*, 19186–19192; c) H. Yan, C. Tian, L. Wang, A. Wu, M. Meng, L. Zhao, H. Fu, *Angew. Chem. Int. Ed.* **2015**, *54*, 6325–6329; *Angew. Chem.* **2015**, *127*, 6423–6427.

[8] A. Katrib, P. Leflaive, L. Hilaire, G. Maire, *Catal. Lett.* **1996**, *38*, 95–99.

[9] a) X. Xie, L. Lin, R.-Y. Liu, Y.-F. Jiang, Q. Zhu, A.-W. Xu, *J. Mater. Chem. A* **2015**, *3*, 8055–8061; b) L. Wu, X. Wang, Y. Sun, Y. Liu, J. Li, *Nanoscale* **2015**, *7*, 5203–5208.

[10] a) Y. Zheng, Y. Jiao, Y. Zhu, L. H. Li, Y. Han, Y. Chen, A. Du, M. Jaroniec, S. Z. Qiao, *Nat. Commun.* **2014**, *5*, 3783–3790; b) J.

Zhuo, T. Wang, G. Zhang, L. Liu, L. Gan, M. Li, *Angew. Chem. Int. Ed.* **2013**, *52*, 10867–10870; *Angew. Chem.* **2013**, *125*, 11067–11070; c) Y. Ito, W. Cong, T. Fujita, Z. Tang, M. Chen, *Angew. Chem. Int. Ed.* **2015**, *54*, 2131–2136; *Angew. Chem.* **2015**, *127*, 2159–2164.

[11] D.-S. Yang, D. Bhattacharjya, S. Inamdar, J. Park, J.-S. Yu, *J. Am. Chem. Soc.* **2012**, *134*, 16127–16130.

[12] C.-Y. Sun, S.-X. Liu, D.-D. Liang, K.-Z. Shao, Y.-H. Ren, Z.-M. Su, *J. Am. Chem. Soc.* **2009**, *131*, 1883–1888.

[13] a) L. Lux, K. Williams, S. Ma, *CrystEngComm* **2015**, *17*, 10–22; b) S.-L. Li, Q. Xu, *Energy Environ. Sci.* **2013**, *6*, 1656–1683.

[14] D.-Y. Du, J.-S. Qin, S.-L. Li, Z.-M. Su, Y.-Q. Lan, *Chem. Soc. Rev.* **2014**, *43*, 4615–4632.

[15] a) J. Li, Y. Chen, Y. Tang, S. Li, H. Dong, K. Li, M. Han, Y.-Q. Lan, J. Bao, Z. Dai, *J. Mater. Chem. A* **2014**, *2*, 6316–6319; b) J.-S. Li, S.-L. Li, Y.-J. Tang, M. Han, Z.-H. Dai, J.-C. Bao, Y.-Q. Lan, *Chem. Commun.* **2015**, *51*, 2710–2713.

[16] Y. Liu, S. Liu, S. Liu, D. Liang, S. Li, Q. Tang, X. Wang, J. Miao, Z. Shi, Z. Zheng, *ChemCatChem* **2013**, *5*, 3086–3091.

[17] a) D. A. Dikin, S. Stankovich, E. J. Zimney, R. D. Piner, G. H. B. Dommett, G. Evmenenko, S. T. Nguyen, R. S. Ruoff, *Nature* **2007**, *448*, 457–460; b) X. Huang, X. Qi, F. Boey, H. Zhang, *Chem. Soc. Rev.* **2012**, *41*, 666–686.

[18] a) T. F. Jaramillo, K. P. Jørgensen, J. Bonde, J. H. Nielsen, S. Horch, I. Chorkendorff, *Science* **2007**, *317*, 100–102; b) N. Pentland, J. O. M. Bockris, E. Sheldon, *J. Electrochem. Soc.* **1957**, *104*, 182–194; c) W. Sheng, H. A. Gasteiger, Y. Shao-Horn, *J. Electrochem. Soc.* **2010**, *157*, B1529–B1536.

[19] a) M. A. Lukowski, A. S. Daniel, F. Meng, A. Forticaux, L. Li, S. Jin, *J. Am. Chem. Soc.* **2013**, *135*, 10274–10277; b) J. D. Benck, Z. Chen, L. Y. Kuritzky, A. J. Forman, T. F. Jaramillo, *ACS Catal.* **2012**, *2*, 1916–1923.